Published in IET Microwaves, Antennas & Propagation
Received on 30th April 2009
Revised on 23rd September 2009
doi: 10.1049/iet-map.2009.0240

In Special Issue on Asia-Pacific Microwave Conference

ISSN 1751-8725

Efficient shooting and bouncing ray tracing using decomposition of wavefronts

V. Mohtashami A.A. Shishegar

Department of Electrical Engineering, Sharif University of Technology, Tehran, Iran
E-mail: shishegar@shafif.edu

Abstract: A new acceleration technique is presented for shooting and bouncing ray tracing in indoor environments. Tracing just a few rays, the algorithm finds the solid angles around the transmitter that transport electromagnetic power to the receiver. The accuracy is then improved by iteratively increasing the tessellation frequency of the source in the power-transporting solid angles. No rays will be sent through non-power-transporting solid angles, which results in significant reduction of the simulation time. An example of applying the method for studying indoor radio wave propagation is presented and the results are compared with a very high-resolution fully three-dimensional (3D) ray tracing simulation as the reference solution. It is observed that power-transporting solid angles constitute only a small fraction of the total space around the source through which the rays are launched. Therefore a high gain in terms of computational efficiency (about 680% saving in the simulation time) is achieved. Furthermore, concurrent application of the proposed method and binary space partitioning method is shown to be possible, which results in a very efficient ray tracing with about 1080% saving in simulation time.

1 Introduction

The study of radio wave propagation is an essential part of designing wireless communication networks in indoor environments. Over the past two decades, ray tracing has been widely used to predict signal characteristics in indoor environments [1–7]. It is basically the application of geometrical optics (GO). In traditional shooting and bouncing ray tracing (SBR), the source is modelled with a finite number of rays shooting out from the transmitting antenna. The algorithm finds the closest wall visible to each ray and calculates the reflected and transmitted rays afterwards. The multi-path rays are detected if their wavefronts illuminate the location of the receiver [1, 7].

The SBR method suffers from large computational time as well as large amount of required memory for keeping track of the rays. This drawback becomes more severe when high accuracy is required and the source must be modelled with a large number of rays. Several acceleration techniques have been proposed since the introduction of the SBR method. These acceleration techniques generally apply geometrical algorithms to reduce the number of required intersection tests of the rays with the objects in the environment. For instance, in [8] the binary space partitioning (BSP) and in [9, 10] the bounding boxes are used, whereas [11] and [12] accelerate the SBR method by tessellating the environment using rectangular and triangular meshes, respectively.

A new acceleration technique for the SBR method has been presented by the authors in the Asia–Pacific Microwave Conference [13], which unlike the previously proposed methods in the literature does not try to reduce the number of intersection tests; rather, it focuses on tracing only the rays that contribute to the total electromagnetic field at the receiver. The basic idea behind this method is to find the solid angles around the transmitter that transport electromagnetic power to the receiver and then tracing the rays in those angles with high resolution. This preliminary idea is now extended to a complete study to evaluate the amount of speedup obtained by applying this method. Specifically, different decomposition schemes are studied in this paper and their computational efficiencies are discussed. Through detailed quantitative discussion, a decomposition scheme that yields the best speedup is selected. A criterion for selecting the

initial resolution of the source is also presented. Moreover, concurrent application of our proposed method and BSP method is shown to be possible, which results in a very efficient ray tracing.

This paper is organised as follows. The proposed acceleration technique is presented in Section 2. Numerical results, complexity analysis and processing gain in terms of simulation time are reported in Section 3. Conclusions are given in Section 4.

2 Proposed acceleration technique

So as to uniformly generate the rays in all directions of the three-dimensional (3D) space, an icosahedron is inscribed in the unit sphere around the source [1]. A typical icosahedron that has 12 vertices, 20 equilateral triangular faces and 30 edges is depicted in Fig. 1*a*. Each edge of the icosahedron is divided into N equal segments. Then, lines parallel to the edges are drawn and form a tessellated face as shown in Fig. 1*b* for $N = 4$. The parameter N is called the tessellation frequency. The 'source rays' are launched in the direction from the source location to the vertices that are generated on the icosahedron faces. As a result, a total number of $10N^2 + 2$ source rays are uniformly generated with hexagonal wavefronts and nearly identical angular separation.

If the source is not modelled with a high enough tessellation frequency, the 'inaccurate path problem' will occur. In order to illustrate the inaccurate path problem, let us consider a simple 2D case as shown in Fig. 2. Suppose that the ray labelled r_0 is sent out from the transmitter, which is located at point O, and let $\angle AOB$ denote the solid angle it represents. This solid angle is relatively large, which implies that the source is modelled with a rather low resolution. The ray r_0 reaches the receiver via a single bounce at wall 1 which is modelled as a lossy dielectric slab. Let r_0' and $\angle AO'B$ represent the reflected ray and corresponding reflected solid angle, respectively. Since the receiver falls within $\angle AO'B$, the ray r_0' is detected and its contribution to the total electromagnetic field at the

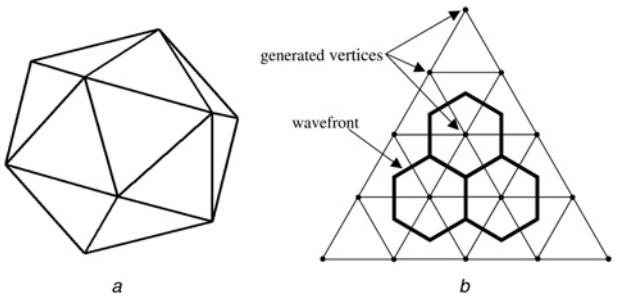

Figure 1 *Source model*

a Typical icosahedron with 20 equilateral triangular faces
b Tessellation of one face with the tessellation frequency of $N = 4$

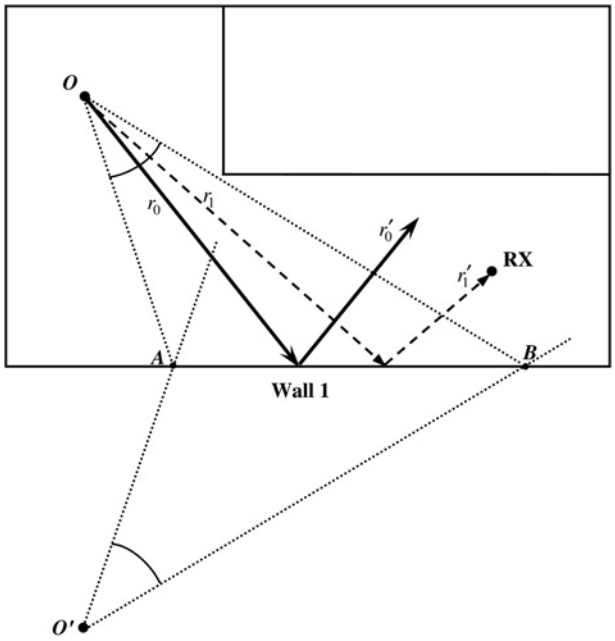

Figure 2 *Inaccurate path problem*

receiver is considered. However, the exact path from the transmitter to the receiver is through ray r_1 that reaches the receiver after being reflected by wall 1. This path difference introduces amplitude and phase errors in the received field. This is because the incident angle of r_0 at intersection with wall 1 (which is calculated by the ray tracing program) is different from the incident angle of r_1 (which is the correct incident angle). Therefore the reflection coefficient, which is a function of the incident angle, is calculated inaccurately. Since the reflection coefficient of a lossy dielectric slab is generally a complex value, the received field contains both amplitude and phase errors. Similar statements can also be said if a transmitted ray, instead of a reflected ray, reaches the receiver. To obtain a better insight, let us consider a 12 cm thick brick wall that has a relative dielectric permittivity of $\varepsilon_r = 5.20 - j0.21$ at 2.44 GHz [14]. The magnitude and phase of the reflection and transmission coefficients as function of incident angle are depicted in Figs. 3*a*–3*d* for TE and TM polarisations. As the incident angle approaches the grazing angle, or near the Brewster angle, the slope of the curves becomes very steep especially for TM polarisation. This means that even a slight error in the incident angle can impose a significantly large error in the reflection and/or transmission coefficients. In typical indoor scenarios a ray may reach the receiver after several reflections and transmissions. Thus, if its path towards the receiver is inaccurate, the reflection and transmission coefficients are computed inaccurately causing significant amplitude and phase errors in the received field. The solution to this problem is to simply increase the tessellation frequency of the source such that the source is modelled with a large number of rays. This overcomes the inaccurate path problem because each ray will now represent a much smaller solid angle. However, the simulation time, which is

doi: 10.1049/iet-map.2009.0240

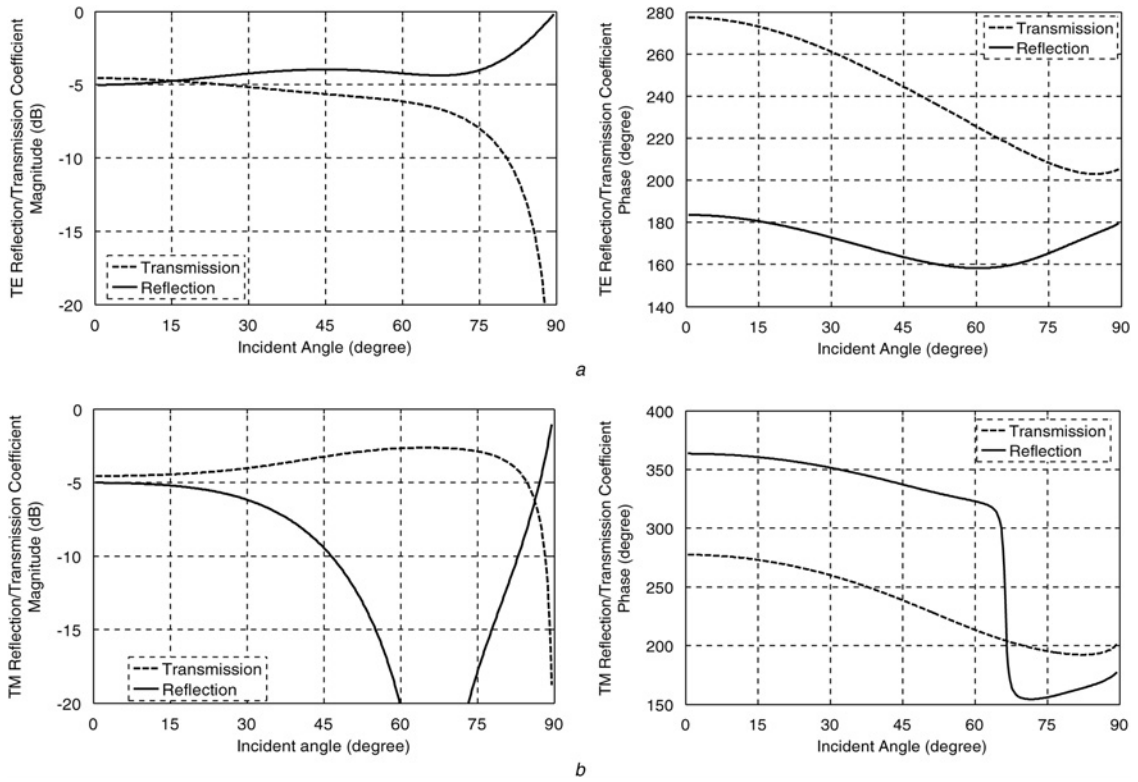

Figure 3 *Magnitude and phase of the reflection and transmission coefficients as functions of incident angle for a 12 cm thick brick wall with a relative dielectric permittivity of* $\varepsilon_r = 5.20 - j0.21$ *at 2.44 GHz*

a TE polarisation
b TM polarisation

a linear function of the number of source rays, will increase. In the rest of this section, we will present a very efficient algorithm that eliminates amplitude and phase errors at computationally affordable cost.

The solid angles around the transmitter that transport electromagnetic power to the receiver constitute only a small fraction of the total space through which the rays are launched. If these solid angles are somehow specified prior to the start of the high-resolution ray tracing, the rays will be launched only through them and the computational burden decreases significantly. Therefore the problem reduces to finding these 'power-transporting' solid angles.

In order to find the power-transporting solid angles, we use an iterative algorithm. The algorithm starts a low-resolution ray tracing and hence, its simulation time is very low. It then finds the detected rays at the receiver. Each detected ray is a part of the binary tree generated by a source ray as the root. The term 'binary tree' refers to the tree-like sequence of rays generated by a source ray at consecutive intersections with the walls of the environment. This root has transported the transmitter power to the receiver by one of its sticks or leaves. Hence, its solid angle contributes to the total electromagnetic field at the receiver. Note that the number of power-transporting source rays is usually much less than the total number of launched source rays. Next, the algorithm decomposes the wavefronts of power-transporting source rays to similar smaller wavefronts. As we discussed above, smaller wavefronts represent smaller solid angles and higher tessellation frequency. This will enhance the correction of the paths towards the receiver and reduces the phase and amplitude errors in the reflection and transmission coefficients. Then the ray tracing algorithm traces the newly generated source rays corresponding to these smaller wavefronts and finds the detected rays at the receiver. The power-transporting source rays corresponding to these smaller wavefronts are then determined from the detected rays. Then the above procedure (decomposition of wavefronts and tracing the newly generated higher resolution source rays) is iteratively repeated until a high enough predefined tessellation frequency (N_{final}) is met. Note that the total number of source rays that are traced at all iterations of our algorithm is much less compared to the total number of source rays that should have been traced if a complete ray tracing were to be performed with N_{final}. Thus, runtime saving is achieved.

The choice of decomposition scheme determines the computational burden of the algorithm. Note that in the SBR method, the circumscribed circle around the hexagonal wavefront of each ray is considered to be the effective wavefront of that ray [1]. The effective wavefront is used for ray detection test at the receiver. For a specific

ray, with the separation angle of α, the radius and the area of the effective wavefront are, respectively, linear and quadratic functions of α [1]. The total number of generated source rays equals $10N^2 + 2$, which is almost proportional to the square of the tessellation frequency for typical values of N. Thus, the area of effective wavefront has $1/N^2$ dependence, which means that its radius and the separation angle have $1/N$ dependence. For instance, if we double the tessellation frequency, four times new source rays are generated. The area of effective wavefront of each newly generated source ray is 1/4 of the area of wavefront of a source ray with old tessellation frequency. Fig. 4 suggests three methods to decompose a circular wavefront to similar smaller wavefronts. Keep in mind that we must not miss any part of effective wavefront of the detected source ray. Moreover, the number of new wavefronts should not be very high such that each iteration of the above algorithm will have an acceptable computational burden. In the rest of this section, we will determine the computational efficiency of these three suggested decomposition schemes.

We define the 'increment coefficient' as the total number of newly generated source rays after decomposition to the number of decomposed wavefronts. For instance, the increment coefficients corresponding to Figs. 4*a*–4*c* are 4, 6 and 7, respectively. The less the increment coefficient is, the less number of rays to be traced in the next iteration of the algorithm. However, the increment coefficient alone cannot characterise the efficiency of a decomposition scheme. We must take into account the amount of the increment in the tessellation frequency (resolution) as well. To do this, we define the 'decomposition efficiency' as the ratio of the optimal value of the increment coefficient to its real value. Since the area of the effective wavefront has $1/N^2$ dependence, the optimal value of the increment coefficient equals the square of the ratio of the radius of large wavefront to the radius of smaller wavefronts. Therefore the optimal values of increment coefficients of Figs. 4*a*–4*c* are 2, 3 and 4, respectively. Thus, the decomposition efficiency of these schemes equals 50, 50 and 57%, respectively. The more the value of decomposition efficiency is, the more optimal the decomposition scheme is. Therefore all three decomposition schemes of Fig. 4 are in general inefficient. The partial overlap of the large wavefront with the small wavefronts has caused the reduction of the decomposition efficiency from its optimal value. However, as we will see later in this section, the decomposition efficiency of Fig. 4*c* is much higher resulting in a nearly optimal decomposition.

By further investigation of Fig. 4*c*, it is observed that the centre of the large power-transporting wavefront lies exactly on the centre of the totally overlapped small wavefront behind it. This means that the ray corresponding to this small wavefront is exactly the same as that of the dark wavefront. Since the ray of the dark wavefront had been traced in the last iteration of the algorithm, it is not necessary to trace the small wavefront in the new iteration. Thus, the increment coefficient reduces to 6 and the decomposition efficiency increases to 67%.

The decomposition scheme of Fig. 4*c* may be interpreted with another point of view. Suppose that we have modelled the source with $N = 4$ in the last iteration of the algorithm and the dark wavefront in Fig. 5*a* has been found to be power-transporting. At the start of the new iteration, the tessellation frequency is doubled to $N = 8$ to achieve higher resolution as shown in Fig. 5*b*. The wavefronts of the newly generated source rays are the small hexagons and are lightly shaded. The dark power-transporting wavefront is also shown in this figure. If we draw the circumscribed circles around the dark wavefront and lightly shaded small wavefronts, Fig. 4*c* is exactly obtained. Hence, the decomposition scheme of Fig. 4*c* can be viewed as generating source rays with twice tessellation frequency and then selecting those that overlap, even partly, with power-transporting solid angles.

With this new point of view, it can be observed that the increment coefficient is a descending function of the number of adjacent power-transporting solid angles. For instance, suppose that all three wavefronts of the interior vertices of Fig. 5*a* have been marked as power-transporting. If the tessellation frequency is doubled as shown in Fig. 6,

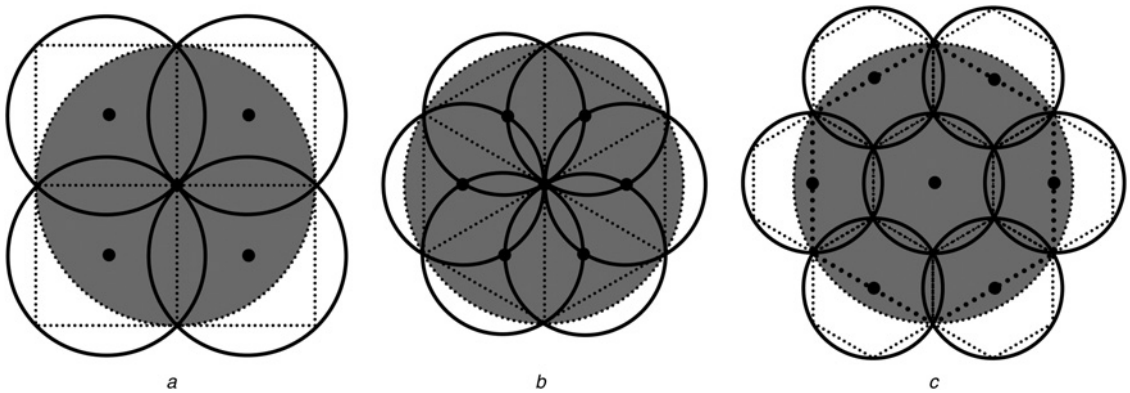

Figure 4 *Suggested decomposition schemes*

doi: 10.1049/iet-map.2009.0240

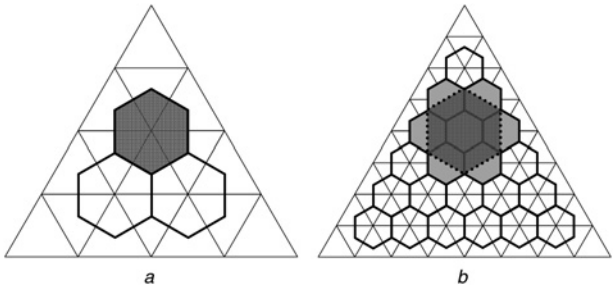

Figure 5 *Decomposition scheme of Fig. 4c with another point of view*

only 15 rays must be traced in the next iteration. This means an increment coefficient of 5. Thus, the decomposition efficiency is further improved to 80%. We will see in the next section that for typical indoor environments, doubling the tessellation frequency leads to an increment coefficient around 4.5. As a result, the decomposition efficiency is enhanced to about 90% resulting in an acceptable computational burden.

3 Numerical results

An indoor scenario is presented in Fig. 7, which shows the first floor of a building formed by two identical storeys [14]. A vertically polarised half-wavelength dipole antenna operating at 2.44 GHz and radiating 10 mW is used as the transmitter. It is located in Room 1 at point ($x = 3.08$ m, $y = 4.52$ m and $z = 2.6$ m). The electrical properties of the materials and thicknesses of the slabs used in the simulation are given in Table 1 according to [14]. Fifty equidistant points along the line at ($x = 6.5$ m, $4\text{ m} < y < 12$ m, $z = 1.2$ m) are considered as receiving locations. The line includes both line-of-sight and non-line-of-sight points. In our iterative algorithm, the initial tessellation frequency of the source is selected $N_0 = 15$, which is doubled at each iteration. The decomposition algorithm and the following tracing procedure is repeated three times resulting in a final tessellation frequency of $N_{\text{final}} = 120$. A fully 3D ray tracing simulation with a tessellation frequency of $N = 120$ is considered as the

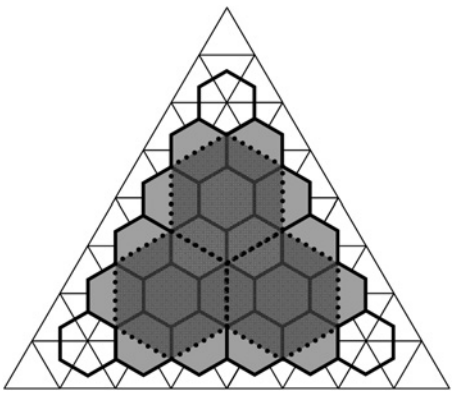

Figure 6 *Decomposition efficiency is enhanced when adjacent solid angles are detected at the receiver*

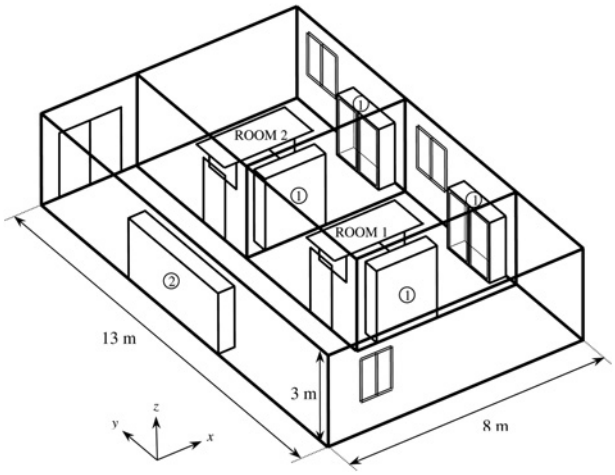

Figure 7 *Plan of the first floor of a building formed by two identical storeys [14]*

The transmitter is located in Room 1 just above the door

reference solution. To obtain accurate results, the termination threshold for ray's amplitude is taken to be 50 dB below the highest amplitude of the generated source rays; that is, if the magnitude of the electric field of a ray falls below the threshold, it will not be traced further. The results including simulation time enhancement of our algorithm with respect to the reference solution are summarised in Table 2. These results are obtained by running a MATLAB code using a PC with 3 GHz Intel Core 2 Duo processor and 4 GBs of RAM. The simulation time of the reference solution was about 2 h and 9 min. Note that the value of the simulation time of the reference solution is high because all 144 002 emitted source rays are traced. More than 5 million rays are generated at the end of the tracing procedure by selecting the above termination threshold. A high speedup in the simulation time is obtained according to Table 2. The decomposition efficiency is 88%, which indicates a nearly optimal decomposition scheme. Note that the absolute simulation time is highly dependent on the termination threshold, electrical properties and losses of the walls and the characteristics of the computer used for simulations. Thus, we emphasise on the simulation speedup in this paper. Fig. 8 shows the electric field magnitude and root mean

Table 1 Material properties and slab thicknesses [14]

	ε_r	σ, mS/m	Thickness, cm
ceiling/floor	7.9	89	25.0
external brick wall	5.2	28	22.0
internal brick wall	5.2	28	12.0
wooden door/cabinet/table	3.0	0	4.0
glass window	3.0	0	0.5

Table 2 Simulation speedup and difference characteristics of our proposed method compared to the reference solution

number of receiving locations	50
total number of traced source rays in reference solution	144 002
total number of traced source rays in proposed method	20 208
simulation speedup	679%
average increment coefficient	4.55
decomposition efficiency	88%
$RMSE_{E\text{-field}}$	0.76 dB
$RMSE_{\tau,\ rms}$	0.25 ns

square (rms) delay spread computed at the receiving locations using our proposed method and the reference solution. Excellent agreement between the curves is observed. There is, however, a little difference between the results. The source of the difference will be discussed later in this section.

To characterise the difference between the results of our proposed iterative algorithm and the reference solution, the difference between the two curves in Fig. 8*a* as well as Fig. 8*b* is averaged using root mean square error (RMSE) defined as

$$\mathrm{RMSE}_{E\text{-field}} = \left[\frac{1}{M}\sum_{m=1}^{M}(|\boldsymbol{E}_{\mathrm{R}}^{m}| - |\boldsymbol{E}_{\mathrm{P}}^{m}|)^2\right]^{1/2} \quad (1)$$

$$\mathrm{RMSE}_{\tau,\mathrm{rms}} = \left[\frac{1}{M}\sum_{m=1}^{M}(\tau_{\mathrm{R}}^{m} - \tau_{\mathrm{P}}^{m})^2\right]^{1/2} \quad (2)$$

where $\mathrm{RMSE}_{E\text{-field}}$ and $\mathrm{RMSE}_{\tau,\mathrm{rms}}$ are, respectively, the RMSE of the electric field magnitude and rms delay spread of our iterative algorithm with respect to the reference solution. M is the number of receiving locations and $(\boldsymbol{E}_{\mathrm{R}}^{m}, \tau_{\mathrm{R}}^{m})$ and $(\boldsymbol{E}_{\mathrm{P}}^{m}, \tau_{\mathrm{P}}^{m})$ denote the total electric field vector and rms delay spread at the mth receiving location computed by the reference solution and our proposed acceleration technique, respectively. As we can see in Table 2, the RMSE for electric field magnitude is less than 1 dB and the RMSE of rms delay spread is only 0.25 ns. This indicates a very good agreement between the results.

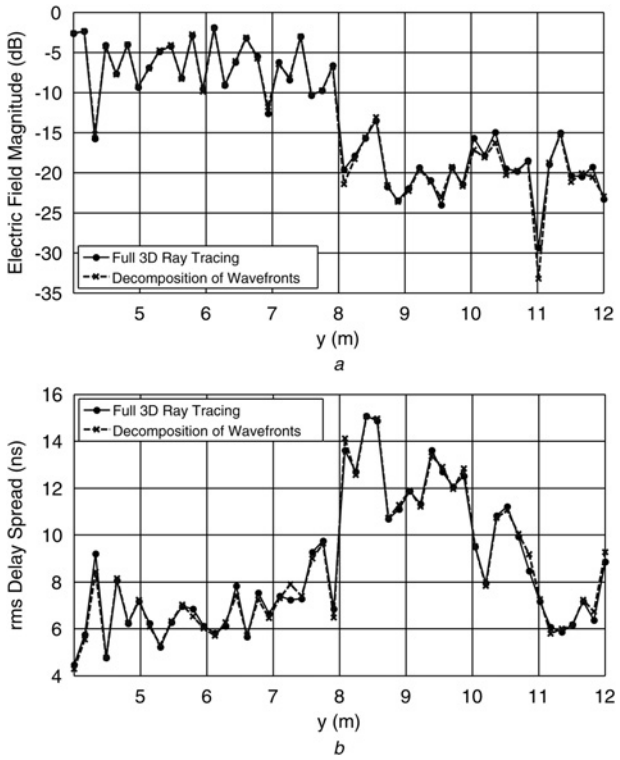

Figure 8 *Simulation results of the method of decomposition of wavefronts compared to the reference solution*

a The electric field magnitude
b rms delay spread

An interesting feature of wavefront decomposition method is that it can be combined with other acceleration techniques that are based on reducing the number of intersection tests such as the widely used BSP method [9]. The reason is that our proposed method tries to reduce the number of launched source rays through an intelligent sampling of the 3D space around the transmitter, whereas the BSP method tries to reduce the number of intersection tests for each launched ray. Therefore there will be no conflict if these two acceleration techniques are applied simultaneously. To compare the speedups obtained by using the two methods and show their consistency in simultaneous application, the above simulation is performed in three different situations. First, only the BSP method is used. Second, only the method of decomposition of wavefronts is used. Third, the two methods are applied concurrently. The speedups are given in Table 3. It is observed that the method of decomposition of wavefronts outperforms the BSP method by a factor of more than 4. Furthermore, when the two methods are applied simultaneously, the overall speedup is a little less than product of the two individual speedups. The reason is that some parts of the method of decomposition of wavefronts such as ray detection test and wavefront decomposition are independent of tracing procedure and are not affected by BSP. However, the concurrent application of the two methods is shown to be

Table 3 Simulation speedups obtained by using BSP and method of decomposition of wavefronts

Acceleration technique	Simulation speedup
BSP	162%
decomposition of wavefronts	679%
BSP + decomposition of wavefront	1080%

doi: 10.1049/iet-map.2009.0240

an effective tool of performing an efficient ray tracing simulation.

The little difference between the results of the method of decomposition of wavefronts and the reference solution as observed in both Figs. 8*a* and 8*b* is because of 'large wavefront problem' already mentioned in the literature [15, 16]. Fig. 9 shows two possible ways in which power–transporting rays may be missed. In this figure, 2D cases are depicted for simplicity. Suppose that the ray labelled r_0 is a low-resolution ray sent out from the transmitter and let $\angle AOB$ denote the solid angle it represents. Suppose that increasing the tessellation frequency of the source will generate the rays r_i, $i = 1, 2, 3, 4$, within this solid angle as well. As shown in Fig. 9*a*, the rays r_i, $i = 1, 2, 3$, hit wall 1, just as r_0 does, whereas r_4 hits wall 2. Therefore the sequence of walls encountered by r_4 is different from that of r_0. If, by any chance, r_0 is not detected at the receiver in the initial iterations of the method of decomposition of wavefronts, the ray r_4 will be suppressed from the list of the rays to be traced in the next iteration. Since the wall sequence encountered by r_4 is not the same as that of r_0, it may be detected at the receiver if being traced. But the method of decomposition of wavefronts does not trace this ray. In Fig. 9*b*, r_0 is not detected at the receiver because of the visibility test failure. Hence, its solid angle will not be considered in the next step of the algorithm. In high-resolution ray tracing, however, r_4 is detected at the receiver. In both cases, power-transporting solid angles are missed because their wavefronts are very large. This problem has been fully solved by using adaptive ray tube tracing (ADRTT) method [15] or ray-beam tracing [16]. In these methods, a ray tube that hits more than one wall is split into several ray tubes such that each newly generated ray tube hits only one wall. We applied these methods on our proposed method and eliminated the difference between the results, but it degraded the simulation speedup significantly. On the other hand, the difference between our proposed method results and the reference solution is very small and can absolutely be neglected for engineering purposes. Therefore it is suggested that our proposed method be performed without ADRTT or ray-beam tracing techniques. Instead, the initial tessellation frequency of the source should be selected properly (neither very low nor very high). A subjective criterion can be made to choose a proper value for initial tessellation frequency. As discussed above, the cause of missing power-transporting solid angles is that the wavefronts of rays are large in initial iterations of our proposed algorithm. If the missing ray has significant power (which happens when the ray is reflected by a strong reflector), the error in the results will increase. Therefore if the wavefronts of the rays are small compared to the area of strong reflectors of the environment such as metallic facets, the difference between the results of wavefront decomposition algorithm and the reference solution will be decreased. This criterion can mathematically be represented as

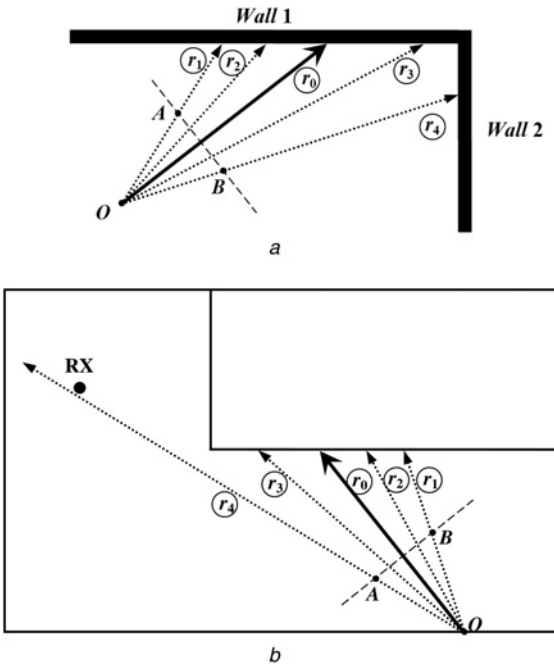

Figure 9 *Two possible ways of missing power-transporting solid angles*

a Encountering different wall sequences
b Visibility test failure

$$\pi\left(\alpha d/\sqrt{3}\right)^2 \ll S \tag{3}$$

where $\alpha d/\sqrt{3}$ is the radius of the wavefront of a ray with a travelled distance d and the separation angle α, and S denotes the area of the a strong reflector facet. Given d and S, an upper bound for α and hence a lower bound for initial tessellation frequency can be found. For instance, the strong reflector of the simulated environment of Fig. 7 is the metallic cabinet in the hallway, which contributes to the received field because the frequency is not very high and the penetration of electromagnetic waves inside the walls is significant. The area of the smallest facet of the metallic cabinet is $S = 1\ \text{m}^2$ and is located about $d = 3$ m away from the source. If '$\ll$' in (3) is interpreted to be 'less than one-tenth', the upper bound for α is found to be 0.103 rad or 5.90°. This value is equivalent to the tessellation frequency of about $N = 11$. Thus, in order to reach the final tessellation frequency of $N_{\text{final}} = 120$ by doubling the tessellation frequency at the end of each iteration, the initial tessellation frequency is selected $N_0 = 15$.

It is obvious that the selection criterion of initial tessellation frequency as described by (3) is totally subjective; it depends on the definition of the 'area' of the 'strong reflector'. However, it provides a rule of thumb for selecting a proper value for the initial tessellation frequency of the source.

4 Conclusions

A new acceleration technique for the ray tracing algorithm was presented in this paper. Instead of reducing the number of

intersection tests, our proposed method finds the solid angles around the transmitter that transport electromagnetic power to the receiver. Then, high-resolution rays are sent out only in these solid angles and the procedure continues iteratively. Since a few rays are traced in each iteration, high resolution can be achieved within acceptable amount of time. The simulation results indicated a very good speedup of about 680% with very little difference between the results of our proposed method and the reference solution. With proper choice of initial tessellation frequency, the difference can be completely ignored and the results are reliable for engineering purposes. Moreover, concurrent application of our proposed method and the BSP method is shown to be possible, which results in a more efficient ray tracing code.

5 Acknowledgments

The authors would like to thank Iran Telecommunication Research Center (ITRC) for supporting this research under the contract T/500/8524. Special thanks are also given to Mr S. Parsa for providing the authors with BSP codes.

6 References

[1] SEIDEL S.Y., RAPPAPORT T.S.: 'Site–specific propagation prediction for wireless in–building personal communication system design', *IEEE Trans. Veh. Technol.*, 1994, **43**, pp. 879–891

[2] ADANA F.S., BLANCO O.G., DIEGO I.G., ARRIAGA J.P., CÁTEDRA M.F.: 'Propagation model based on ray tracing for the design of personal communication systems in indoor environments', *IEEE Trans. Veh. Technol.*, 2000, **49**, pp. 2105–2112

[3] YANG C.F., WU B.C., KO C.J.: 'A ray–tracing method for modeling indoor wave propagation and penetration', *IEEE Trans. Antennas Propag.*, 1998, **46**, pp. 907–919

[4] LU W., CHAN K.T.: 'Advanced 3D ray tracing method for indoor propagation prediction', *Electron. Lett.*, 1998, **34**, (12), pp. 1259–1260

[5] CHEN S.-H., JENG S.-K.: 'An SBR/image approach for radio wave propagation in indoor environments with metallic furniture', *IEEE Trans. Antennas Propag.*, 1997, **45**, pp. 98–106

[6] MOHTASHAMI V., SHISHEGAR A.A.: 'A new double–counting cancellation technique for ray tracing using separation angle distribution'. IEEE Radio Frequency and Microwave (RFM) Conf., Kuala Lumpur, Malaysia, December 2008, pp. 437–441

[7] CÁTEDRA M.F., PÉREZ J., ADANA F.S., GUTIÉRREZ O.: 'Efficient ray–tracing technique for three–dimensional analyses of propagation in mobile communications: application to picocell and microcell scenarios', *IEEE Antennas Propag. Mag.*, 1998, **40**, (2), pp. 15–28

[8] TORRES R.P., VALLE L., DOMINGO M., LOREDO S.: 'An efficient ray–tracing method for radiopropagation based on the modified BSP algorithm'. IEEE Vehicular Technology Conf. (VTS 50th), Amsterdam, Netherlands, September 1999, **4**, pp. 1967–1971

[9] GLASSNER S.: 'An introduction to ray tracing' (Academic Press, 1989)

[10] GOLDSMITH J., SALMON J.: 'Automatic creation of object hierarchies for ray tracing', *IEEE Comput. Graph. Appl.*, 1987, **7**, (5), pp. 14–20

[11] ZHENGQING Y., ISKANDER M.F., ZHIJUN Z.: 'Fast ray tracing procedure using space division with uniform rectangular grid', *Electron. Lett.*, 2000, **36**, (10), pp. 895–897

[12] ZHENGQING Y., ISKANDER M.F., ZHIJUN Z.: 'A fast indoor/outdoor ray tracing procedure using combined uniform rectangular and unstructured triangular grids'. IEEE Antennas Propagation Soc. Int. Symp., Salt Lake City, UT, July 2000, vol. 2, pp. 1134–1137

[13] MOHTASHAMI V., SHISHEGAR A.A.: 'A new ray tracing acceleration technique based on decomposition of wavefronts'. IEEE Asia Pacific Microwave Conf. (APMC), Hong Kong, December 2008, pp. 1–4

[14] BERNARDI P., CICCHETTI R., TESTA O.: 'An accurate UTD model for the analysis of complex indoor radio environments in microwave WLAN systems', *IEEE Trans. Antennas Propag.*, 2004, **52**, (6), pp. 1509–1520

[15] SUZUKI H., MOHAN A.S.: 'Ray tube tracing method for predicting indoor channel characteristics map', *Electron. Lett.*, 1997, **33**, pp. 1495–1496

[16] RAJKUMAR A., NAYLOR B.F., FEISULLIN F., ROGERS L.: 'Predicting RF coverage in large environments using ray–beam tracing and a partitioning tree represented geometry', *Wirel. Netw.*, 1996, **2**, (2), pp. 143–154

doi: 10.1049/iet-map.2009.0240